




RECENT ADVANCES IN FUNCTIONAL MATERIALS AND 2D/3D PROCESSING FOR SENSORS AND ELECTRONIC APPLICATIONS

Fe Thin Film-Coated Optics for Corrosion Monitoring: Optical and Electrochemical Studies

RUISHU F. WRIGHT ^{1,2,6} RACHEL ENGLISH,^{1,3} JAMES C. EGBU,^{1,3} JOHN BALTRUS,¹ MARGARET ZIOMEK-MOROZ,⁴ and PAUL R. OHODNICKI JR.^{1,5}

1.—National Energy Technology Laboratory, Pittsburgh, PA 15236, USA. 2.—Leidos Research Support Team, Pittsburgh, PA 15236, USA. 3.—Department of Materials Science and Engineering, Carnegie Mellon University, Pittsburgh, PA 15213, USA. 4.—National Energy Technology Laboratory, Albany, OR 97321, USA. 5.—Department of Mechanical Engineering and Materials Science, University of Pittsburgh, Pittsburgh, PA 15261, USA. 6.—e-mail: Ruishu.Wright@netl.doe.gov

Corrosion proxy materials integrated with an optical sensing platform enable a real-time optical corrosion sensor for natural gas pipelines to prevent methane leaks and catastrophic events. Effects of CO₂, pH, and film thickness on corrosion of Fe thin films (25 nm, 50 nm, 100 nm) were studied using optical and electrochemical methods in 3.5 wt.% NaCl solutions at 30°C. An increase in light transmission (*T*%) corresponded to corrosion of Fe thin films. CO₂ accelerated corrosion of Fe thin films because of the lower pH and the promoted corrosion reactions, resulting in a faster increase of *T*% than without CO₂ or at higher pH. While the corrosion rate increased with increasing film thickness, electrochemical corrosion of Fe thin films was in good agreement with that of bulk carbon steel, verifying that Fe thin films can serve as a representative corrosion proxy when integrated with the optical sensing platform.

INTRODUCTION

Corrosion has been a great concern in the oil and natural gas (O&G) industry because it adversely affects the structural infrastructure in exploration, production, processing, and transport of oil and natural gas and can cause significant economic costs and safety issues.^{1–3} Internal corrosion can occur in the natural gas transmission pipelines when aqueous electrolytes are present. Inside the pipelines, electrochemical corrosion takes place in the water phase condensed from wet gas or from liquid water because of upstream plant upsets. The inherently existing acidic gases such as CO₂ and H₂S can dissolve in the water phase forming corrosive electrolytes.⁴ Over the last 30 years, corrosion has caused ~25% of the incidents in natural gas transmission and gathering pipelines, and 61% of corrosion caused incidents were due to internal corrosion, according to the Pipeline and Hazardous

Materials Safety Administration (PHMSA) database.^{5,6} Natural gas constitutes 32% of the energy consumption in the US in 2019 according to the US Energy Information Administration (EIA).⁷ The natural gas delivery system includes 528,000 km (328,000 miles) of natural gas transmission and gathering pipelines.⁸ It has been challenging to monitor internal corrosion effectively as the inside of the pipeline is not readily accessible during regular maintenance and inspection. Moreover, corrosion can occur at some random locations inside and outside pipelines over thousands of miles. Therefore, it is important to locate and monitor corrosion events and corrosive conditions along the long-distance pipeline to effectively mitigate corrosion and ensure safe, secure, and reliable energy transportation.⁹

The ability to monitor internal corrosion in natural gas transmission pipelines before the structural integrity gets compromised could have a significant impact on preventing methane leaks as well as catastrophic events resulting from corrosion.

The fiber optics sensing platform provides many advantages and has been studied for sensing a broad range of chemical and physical parameters, including corrosion monitoring.^{10–19} Compared with other sensing platforms, the fiber optics platform has favorable features such as distributed sensing, non-destructive monitoring, in situ real-time measurements, small size, flexibility, light weight, inherent immunity to electromagnetic interference (EMI), compatibility to optical fiber telecommunication, and improved safety in the presence of flammable gas compared to electrical-based sensors. Spatially distributed monitoring makes the fiber optics sensing particularly suitable for long-distance infrastructures (e.g., pipelines) in the O&G industry, enabling continuous real-time monitoring over the whole structure with location information. To take advantage of fiber optics sensing platform, corrosion proxy sensing materials are a key enabling component.

A recent concept for early corrosion onset detection involves the use of proxy materials integrated with the fiber optics sensing platform, which provides insight into the corrosive conditions in the pipelines. Successful realization of this class of sensors requires a detailed understanding of the corrosion behaviors of the proxy materials. Fe or alloy thin films have been used in corrosion monitoring studies through measurements of electrical resistance or light reflection/transmission of the thin films in NaCl solutions.^{11,20–22} However, there have been few studies on thin film coated optics in CO₂ containing brine solutions, which are more representative of corrosive conditions in natural gas pipelines and other systems in the O&G industry.^{6,23} Therefore, in this work, Fe thin films of different thicknesses (25 nm, 50 nm, 100 nm) were tested in CO₂-saturated 3.5 wt.% NaCl solutions at 30°C. The effects of CO₂, pH, and film thickness were studied using optical transmission measurements and in situ electrochemical methods.

EXPERIMENTAL PROCEDURE

Fe Thin Film Preparation

Three thicknesses of Fe thin films were tested (25 nm, 50 nm, and 100 nm), and a 400-nm-thick film was only used in some electrochemical tests. Fe thin films were prepared by sputter deposition onto one side of the fused quartz disk substrates, Ø 25.4 mm × 1.6 mm (Ø 1 in. × 1/16 in.). The substrates were cleaned with isopropanol and dried before deposition. The deposition was completed with a throw distance of ~ 5.2 cm in a sputter-down configuration. The radio frequency (RF) sputtering was carried out with 200 W power and 10 mTorr Ar pressure. The Fe target was pre-sputtered for 10 min before deposition to remove any undesirable contamination.

Fe Thin Film Characterization

An atomic force microscope (AFM, NT-MDT Solver Next) was used to image the as-received Fe thin films on the substrates. The sample was mounted to steel spacers using adhesive to adjust the height of the sample on the AFM stage. Tap300Al-G tips (BudgetSensors) with a 30-nm aluminum reflex coating and 300-kHz resonance frequency were used in a semi-contact mode to minimize surface wear during scans. Scans were completed at 1 Hz for a 1 µm × 1 µm area.

The Fe thin films were also characterized using x-ray photoelectron spectroscopy (XPS, PHI 5600ci) with a monochromatic Al K α x-ray source. The XPS survey spectra were obtained using the pass energy of 187.85 eV and step size of 0.8 eV. Binding energies were corrected for charging by referencing to the C 1s peak at 284.6 eV. Atomic concentrations were calculated from the XPS spectra using manufacturer-provided sensitivity factors. Ar ion gun sputtering was used to remove adventitious carbon on the top surface and to obtain depth profiles of the films.

Optical and Electrochemical Tests

Figure 1 shows the experimental system assembled in a photo-electrochemical (PEC) flow cell (ZAHNER-elektrik). The Fe-coated quartz disk was mounted as the rear window and sealed with an O-ring. The Fe film facing inward was the working electrode. A piece of copper tape (5 mm × 5 mm) was attached to the Fe film edge without touching the solution. The copper tape was in contact with a patch of conductive cloth on the conducting plate, which was electrically connected to the working electrode terminal through a soldered wire. The counter electrode was a Pt coil pre-installed in the cell and was connected to the counter electrode terminal. The Ag/AgCl reference electrode in 3 M NaCl solution was inserted in the cell as the reference electrode. The measured electrode potential was converted to the standard hydrogen electrode (SHE) scale. This setup allows simultaneous optical and electrochemical measurements.

The flow-cell test solution contained 3.5 wt.% NaCl at 30°C at ambient pressure, which was pumped through the cell at a flow rate of 113 mL/min. Three different solution (Soln.) compositions are listed in Table I. Soln. #1 was the N₂-saturated solution, Soln. #2 was the CO₂-saturated solution, and Soln. #3 was the CO₂-saturated solution with 0.03 molal NaHCO₃ (around pH 6). pH was measured using a Mettler Toledo SevenExcellence pH meter.

The optical transmission through the PEC cell was measured using a spectrophotometer (Ocean Optics Jaz) and an optical power meter (Thorlabs PM100D) simultaneously via a bifurcated cable. The light transmittance ($T\%$) was normalized to a value

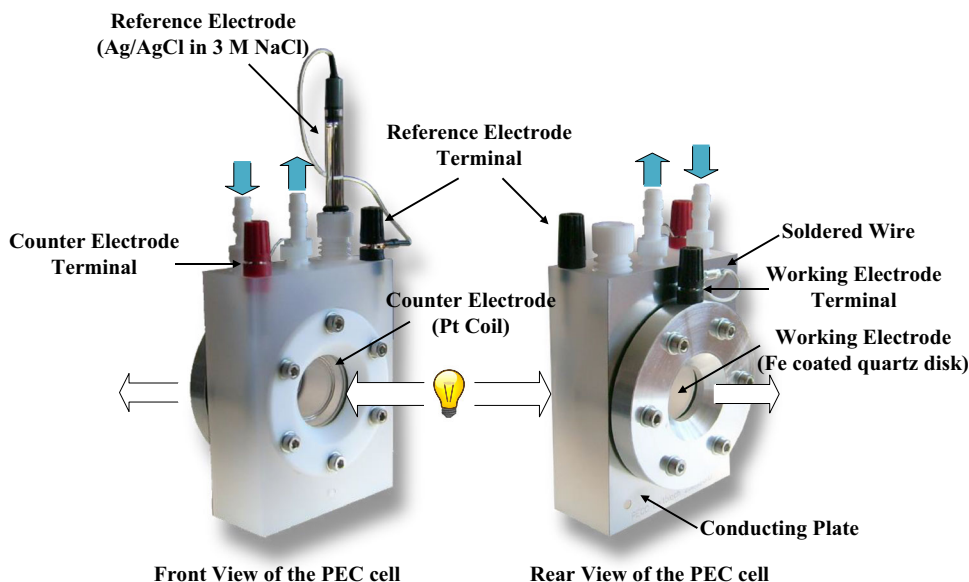


Fig. 1. Experimental setup of the PEC flow cell. Blue arrows represent the solution flow direction at 30°C. White arrows represent the collimated light rays. Adapted from Ref. 6 (Color figure online).

Table I. Modeled solution speciation, pH, and corrosion rates in the test solutions at 30°C⁵

Solution	#1	#2	#3
Gas	N ₂	CO ₂	CO ₂
NaHCO ₃ /(mol/kg H ₂ O)	0	0	0.03
pH-measured	7.31	3.96	6.20
pH-modeled	6.84	3.86	6.15
H ₃ O ⁺ (aq)	1.66 × 10 ⁻⁷	1.55 × 10 ⁻⁴	8.05 × 10 ⁻⁷
OH ⁻ (aq)	1.66 × 10 ⁻⁷	1.77 × 10 ⁻¹⁰	3.41 × 10 ⁻⁸
CO ₂ (aq)	-	2.49 × 10 ⁻²	2.48 × 10 ⁻²
HCO ₃ ⁻ (aq)	-	1.55 × 10 ⁻⁴	3.00 × 10 ⁻²
CO ₃ ²⁻ (aq)	-	2.70 × 10 ⁻¹⁰	1.02 × 10 ⁻⁵
Modeled CR/mm y ⁻¹	0.011	1.72	0.46

of 100% when the Fe thin film was totally dissolved. $T\%$ was calculated following Eq. 1.

$$T\% = (I_{\text{meas}} - I_{0\%}) / (I_{100\%} - I_{0\%}) \quad (1)$$

where I_{meas} is the measured transmitted light intensity through the PEC flow cell, $I_{100\%}$ (light reference) equals I_{meas} when the Fe thin film is totally dissolved, and $I_{0\%}$ (dark reference) equals I_{meas} when the light source is turned off.

The electrochemical tests were performed using a Gamry Reference 600+ potentiostat, including linear polarization resistance (LPR), electrochemical impedance spectroscopy (EIS), and linear sweep voltammetry (LSV). LPR was measured between ± 10 mV versus the corrosion potential (E_{corr}) with a sweep rate of 0.125 mV/s. EIS was performed from 100 kHz to 10 mHz with an amplitude of 10 mV versus E_{corr} . LSV was scanned within ± 300 mV versus E_{corr} with a sweep rate of 1 mV/s. The 400-nm-thick Fe film was used for LSV because thinner films dissolved too quickly to complete the sweep

before the film was gone, especially for anodic sweeps.

In a three-electrode system, when corrosion is under charge transfer control and the working electrode is polarized within a sufficiently small range around E_{corr} , the corrosion current density, j_{corr} , can be calculated according to the Stern-Geary equation, Eq. 2.²⁴⁻²⁷

$$j_{\text{corr}} = (b_c b_a) / [2.303 R_{\text{pol}} (b_c - b_a)] \quad (2)$$

where R_{pol} is the area-specific polarization resistance, and b_c (negative) and b_a (positive) are cathodic and anodic Tafel slopes, respectively. R_{pol} was obtained from LPR and corrected for the solution resistance (R_{sol}) measured from EIS. Tafel slopes were calculated following Eqs. 3 and 4, assuming the symmetry coefficient β to be 0.5.

$$b_a = (2.303RT) / [(1 - \beta)nF] \quad (3)$$

$$b_c = (2.303RT) / [(-\beta)nF] \quad (4)$$

where R represents the gas constant, T is the absolute temperature, F is the Faraday constant, and n is the electron number transferred during corrosion. The corrosion rate (CR) was calculated from j_{corr} following Eq. 5 assuming uniform corrosion.

$$\text{CR} = (j_{\text{corr}}M)/(nF\rho) \quad (5)$$

where M and ρ are the molecular mass and density of Fe, respectively. n was taken as 2 for oxidation from Fe to Fe^{2+} .

RESULTS AND DISCUSSION

CO₂ Corrosion Modeling

The solution speciation, corrosion rates, and Pourbaix diagram were modeled using OLI Analyzer Studio V9.5 based on the mixed-solvent electrolyte model.^{28–30} CR was modeled assuming a rotating disk electrode (RDE) system at 300 rpm. The modeling results in Table I show that addition of CO₂ lowers the pH compared to the N₂-saturated solution, and CO₂(aq) is the dominant carbonate species while HCO₃[−](aq) increases at higher pH in Soln. #3. The modeled pH values were consistent with the measured pH.

The dissolved CO₂ lowers the pH through dissociation of H₂CO₃(aq) and promotes electrochemical corrosion reactions. For cathodic reactions in deaerated conditions, H₂CO₃(aq) could provide an additional hydrogen source for the hydrogen evolution reaction through two levels of dissociation. Direct reduction of non-dissociated H₂CO₃(aq) has also been proposed by some researchers.^{31–35} For anodic reactions, CO₂(aq) was found to participate in oxidation of Fe through formation of an intermediate.^{5,36} The anodic reaction mechanism has been frequently assumed to follow the Bockris mechanism.^{34,37–39}

The model predicts that CR of Fe increases by more than two orders of magnitude in the CO₂-saturated solution (Soln. #2) compared to Soln. #1. The higher pH in Soln. #3 results in a lower CR. The Pourbaix diagram in supplementary Fig. S1 shows that the thermodynamically stable products from CO₂ corrosion are soluble Fe^{2+} (aq) at pH 4 and FeHCO_3^+ (aq) at pH 6, respectively. This indicates active corrosion, and Fe thin films would dissolve in the CO₂-saturated brine solutions.

Fe Thin Film Characterization Results

AFM Results

Figure 2 shows the AFM images of Fe thin films with different thicknesses. The grain size for each sample was determined using the concentric circles method (ASTM E112).⁴⁰ The surface roughness was obtained using Gwyddion software built-in roughness analysis. The average grain size and roughness are listed in Table II, and they increased with the increasing film thickness from 25 nm to 100 nm.

The sheet resistance (R_s) was calculated from the Fe bulk resistivity (R_b , $9.71 \times 10^{-8} \Omega\text{-cm}$) and the film thickness (t) following Eq. 6,⁴¹ and the values are listed in Table II. Apparently, R_s decreases as the film gets thicker.

$$R_s = R_b/t \quad (6)$$

XPS Results

The XPS depth profiles of Fe thin films are depicted in supplementary Fig. S2. Adventitious carbon was sputtered away within 0.1–0.2 nm of the top surface. An oxidized top layer (1.3–1.7 nm thick) was observed because of exposure to air during the sample transport (Table II). The boundary between the oxidized layer and the Fe film bulk was taken at half of the maximum oxygen content. The oxidized top layer can be protective enough to hinder corrosion of the underlying Fe, especially at higher pH, so precathodization of -300 mV versus E_{corr} was applied for < 1 min to remove this layer in some electrochemical tests. As the Fe film was sputtered away, the SiO₂ substrate was revealed. Figure 3 shows the XPS spectrum of the underlying bulk of an Fe thin film, confirming metallic Fe was successfully deposited onto the substrate.

Optical Studies of Fe Thin Film Corrosion

Light Transmittance Calculation

The light transmittance was calculated using standard Fresnel-based models of transmission through a thin film system. For a light-absorbing Fe thin film with a uniform thickness (d_1) on a quartz substrate, the complex refractive index of Fe thin film is written as $n_1 - ik_1$, where n_1 is the refractive index and k_1 is the extinction coefficient. At normal incidence of a parallel beam of light, the transmittance ($T\%$) of the film can be calculated following Eq. 7.⁴² n_0 and n_2 are refractive indices of the solution and the quartz substrate, respectively.

$$T\% = \frac{n_2}{n_0} \frac{e^{2\alpha_1} + (g_1^2 + h_1^2)(g_2^2 + h_2^2)e^{-2\alpha_1} + C \cos 2\gamma_1 + D \sin 2\gamma_1}{\left[(1 + g_1)^2 + h_1^2 \right] \left[(1 + g_2)^2 + h_2^2 \right]} \quad (7)$$

$$\text{where } g_1 = \frac{n_0^2 - n_1^2 - k_1^2}{(n_0 + n_1)^2 + k_1^2}, g_2 = \frac{n_1^2 - n_2^2 + k_1^2}{(n_1 + n_2)^2 + k_1^2}, h_1 = \frac{2n_0k_1}{(n_0 + n_1)^2 + k_1^2},$$

$$h_2 = \frac{-2n_2k_1}{(n_1 + n_2)^2 + k_1^2}, \alpha_1 = \frac{2\pi k_1 d_1}{\lambda}, \gamma_1 = \frac{2\pi n_1 d_1}{\lambda}, C = 2(g_1 g_2 -$$

$$h_1 h_2), D = 2(g_1 h_2 + g_2 h_1).$$

To demonstrate $T\%$ is a function of the Fe film thickness, one example is given in Fig. 4 at the wavelength of 600 nm. n_0 and n_2 were taken as 1.332 (water) and 1.458 (fused quartz).^{43,44} n_1 and k_1 were assumed to be the same as bulk Fe for different thicknesses, $n_1 = 2.328$ and $k_1 = 3.259$.⁴⁵ $T\%$ decreases with increasing Fe film thickness as

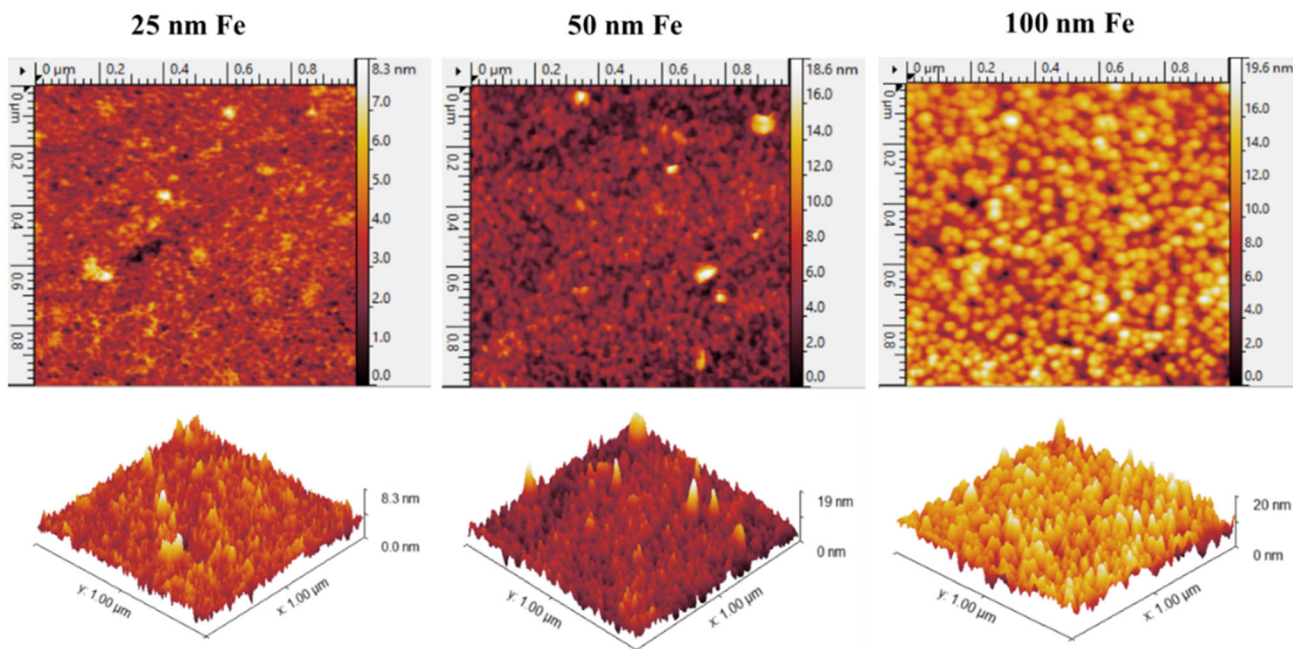


Fig. 2. AFM topography and 3D images for Fe thin films to illustrate the grain sizes and roughness.

Table II. Properties of Fe thin films with different thicknesses

Thickness/nm	25	50	100
Average grain size/nm	1.95	2.88	4.29
Roughness/Ra	1.56	2.22	2.75
Top oxidized layer thickness/nm	1.3	1.6	1.7
Calculated $R_s/(\Omega/\text{sq})$	3.88	1.94	0.97

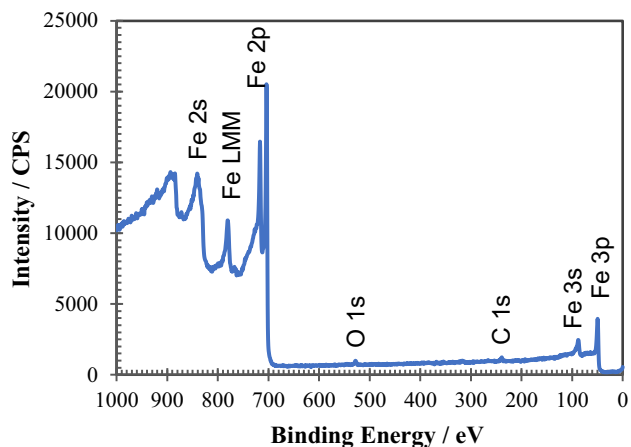


Fig. 3. XPS result for 100 nm Fe thin film after being sputtered to 30 nm depth.

expected, with the strongest dependence occurring for film thicknesses $< \sim 60$ nm as thicker films are substantially opaque. Therefore, $T\%$ through the Fe thin films can serve as a measure of film thickness, which enables an optical sensor to monitor corrosion/mass loss and quantify the CR with Fe thin

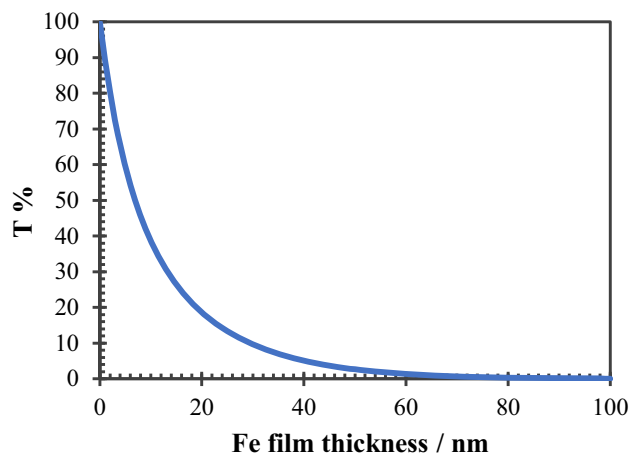


Fig. 4. Calculated transmittance of an Fe thin film as a function of film thickness at the wavelength of 600 nm. Adapted from Ref. 6.

films as a corrosion proxy. In cases where solid corrosion products (e.g., FeCO_3) may be present on the film, it will lead to a different, albeit still effective, sensing mechanism in terms of light transmission, because the corrosion products have a different complex refractive index than Fe.

Light Transmittance Measurements During Corrosion

The measured light transmittance increased as the Fe thin films became thinner during corrosion. Figure 5 shows the transmittance spectra of a 25-nm Fe film exposed to the CO_2 -saturated 3.5 wt.% NaCl solution at 30°C . The spectra showed a broadband $T\%$ response to corrosion between the wavelength of 400 nm and 900 nm, and $T\%$

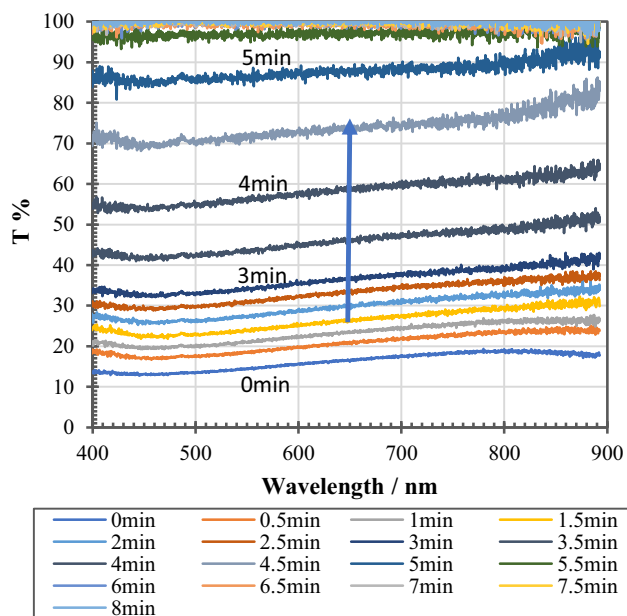


Fig. 5. Optical transmittance spectra of 25 nm Fe thin film over time in CO_2 -saturated 3.5 wt.% NaCl solution at 30°C .

increased over time until the Fe thin film totally dissolved in the solution. It is representative of $T\%$ measurements in all the tests in this work. For the film thickness of 25 nm, the measured $T\%$ at the wavelength of 600 nm before corrosion (at 0 min) was $\sim 15\%$, close to the calculated $T\%$ of $\sim 13\%$ at 25 nm thickness in Fig. 4.

Besides the optical spectra, transmitted light power also increased corresponding to corrosion of Fe thin films. Figure 6 depicts the plots of $T\%$ versus time measured with the optical power meter for different film thicknesses in the three test solutions. All the plots showed first a slow increase (a small slope) and then a sharp increase (a large slope) before the thin films totally dissolved. This followed the pattern of the calculated $T\%$ versus thickness in Fig. 4 with the dependence of transmittance on film thickness growing stronger when the transparency of such films increases.

Comparing the three test solutions, Fe thin films corroded faster in the CO_2 -saturated NaCl solution (Soln. #2) than in the N_2 deaerated solution (Soln. #1) and relatively slower in Soln. #3 with higher pH than in Soln. #2. This is consistent with the CR modeling in Table I. The $T\%$ plots in Soln. #1 were not as smooth as those in Soln. #2 and #3. Some small pieces of undissolved Fe film were observed in the circulating solution deaerated with N_2 , suggesting a tendency for film delamination in addition to thickness reduction due to mass loss in Soln. #1. The CR was much slower in Soln. #1; however, $\text{Cl}^-(\text{aq})$ could promote localized corrosion, weakening the structural integrity of the films.^{46,47} Thus, the Fe thin films became susceptible to delamination under the flow, which caused sudden increases of $T\%$ as small pieces of Fe film fell off. Localized

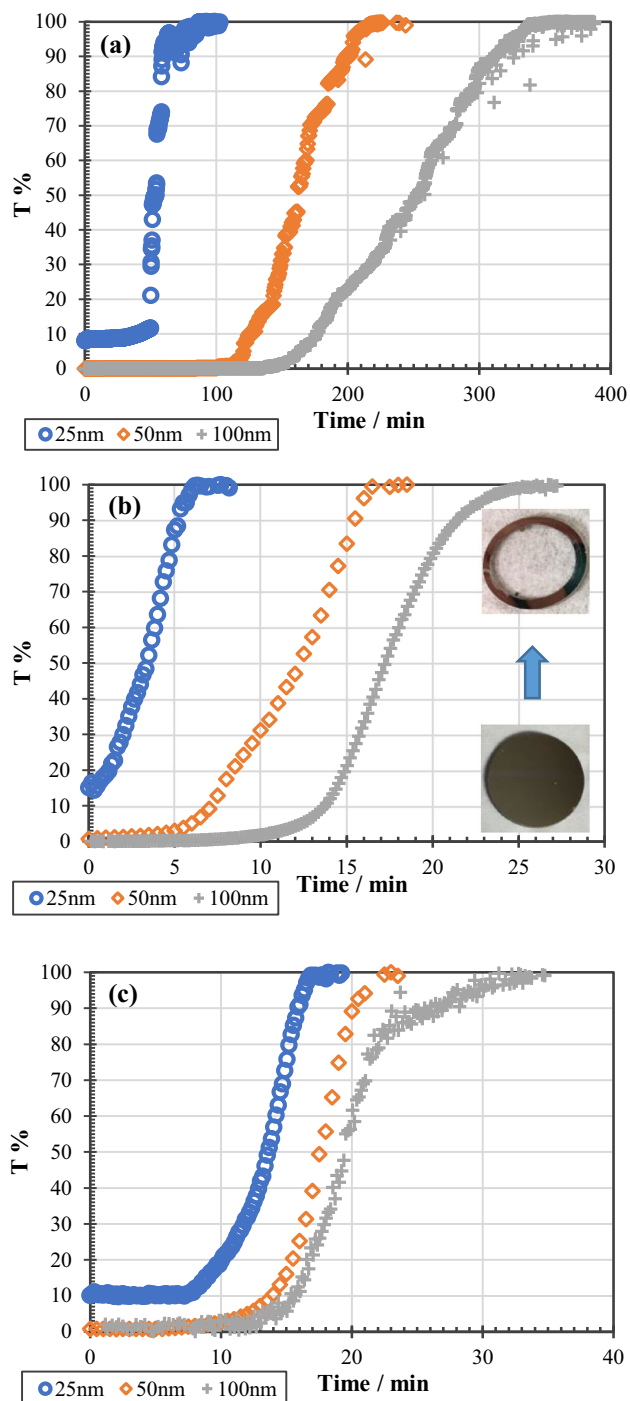


Fig. 6. $T\%$ of different thicknesses of Fe thin films as a function of time at 30°C . (a) Soln. #1: N_2 deaerated NaCl solution, pH 7; (b) Soln. #2: CO_2 -saturated NaCl solution, pH 4; (c) Soln. #3: CO_2 -saturated NaCl solution, pH 6.

corrosion is not as predictable as the general (non-localized) active corrosion. This may explain that the plot slopes in Soln. #1 had a larger difference among different thicknesses than those in the other two solutions.

Naturally, the thicker films took a longer time to get totally dissolved in each solution, but it is important to note that the initial CR was actually

higher for the thicker films as discussed in more detail in the subsequent sections. The total dissolution times of Fe thin films when yielding 100% transmittance are summarized in Table III for comparison.

Electrochemical Studies of Fe Thin Film Corrosion

Table III lists E_{corr} , R_{pol} , and CR of Fe thin films from the electrochemical measurements. In each solution, E_{corr} grew slightly more negative as the film thickness increased from 25 nm to 100 nm, indicating the thicker film was more prone to corrosion. From Soln. #1 to #3, E_{corr} of the Fe thin films generally agreed with E_{corr} of the bulk X65 carbon steel studied in an RDE system.⁵ API 5L X65 carbon steel is commonly used for transmission pipelines, and it is compared with the Fe thin films in Table III.

The electrochemical results showed that CO_2 increased the CR of Fe thin films by more than one order of magnitude, comparing Soln. #2 with Soln. #1. The higher pH in Soln. #3 led to a decrease in CR compared with Soln. #2. This trend is in reasonable agreement with the modeled CR in Table I for the three solutions. The CR increase was caused by the lower pH and the promoted corrosion reactions in the presence of CO_2 .^{34,36,48} The higher pH in Soln. #3 had an opposite effect. Detailed corrosion mechanisms have been discussed in Ref. 5. R_{pol} and CR of Fe thin films in the three solutions resembled the corrosion behaviors of the bulk X65 carbon steel. This resemblance supports that Fe thin films can serve as a corrosion proxy to indicate the corrosion onset and rate of bulk pipeline steel. Additionally, as the films are much thinner than the corresponding bulk materials, they will yield a significant change in optical transmission long before significant amounts of pipeline material have corroded, capable of monitoring early corrosion onset.

The electrochemical CR was observed to increase with increasing thickness in each solution (Table - III). From 25 nm to 100 nm Fe, CR increased by a factor of 6.5, 1.9, and 2.3 in Soln. #1, #2, and #3, respectively. A similar correlation between CR and film thickness was also reported in an aerated NaCl solution previously.⁴⁹ As shown in Table II, the morphology and R_s of Fe films varied with thickness. Although a smaller grain size in the thinner film may lead to a higher CR,⁵⁰ the thicker film has greater surface roughness and a lower R_s , which can accelerate corrosion.⁵¹ In general, CR of Fe thin film was close to that of the bulk carbon steel in each solution, and the slight discrepancy could be explained by the difference in experimental configurations between the PEC flow cell and the RDE system.

The total dissolution time was calculated from the electrochemical CR, assuming it was the average

Table III. E_{corr} , R_{pol} , CR, and total dissolution time of Fe thin films compared with bulk carbon steel (CS)⁵

Thickness/nm	Soln. #1 (N ₂)			Soln. #2 (CO ₂ , pH 4)			Soln. #3 (CO ₂ , pH 6)					
	25	50	100	Bulk CS	25	50	100	Bulk CS	25	50	100	Bulk CS
E_{corr}/V versus SHE	-0.484	-0.529	-0.545	-0.547	-0.528	-0.535	-0.541	-0.494	-0.540	-0.547	-0.543	-0.534
$R_{\text{pol}}/\Omega \text{ cm}^2$	7659	3184	1212	1323	131	73	65	102	159	103	70	174
CR/mm y ⁻¹	0.020	0.048	0.13	0.12	1.2	2.1	2.3	1.49	0.95	1.5	2.2	0.87
Dissolution time from CR/min	657	548	404	-	11	13	23	-	14	18	24	-
Dissolution time from T%/min	82	217	344	-	6	17	26	-	17	24	32	-

CR throughout the process, and is compared with the dissolution time obtained from light power measurements in Fig. 6. In Soln. #2 and #3, the dissolution times were in good agreement between these two types of measurements. In Soln. #1, the electrochemical CR indicated a longer corrosion process than the optical measurements. The reason could be that general corrosion was assumed for electrochemical measurements while localized/pitting corrosion and erosion probably occurred in Soln. #1, causing mechanical delamination of the Fe films that could not be fully measured electrochemically.

The EIS results confirmed active corrosion of Fe thin films in CO₂-saturated NaCl solution (Soln. #2). Figure 7a shows that the Nyquist plots were suppressed semicircles with one time constant, which were fitted with a Randle circuit without diffusion. R_{pol} obtained from EIS was consistent with that from LPR. In the Bode plots (Fig. 7b), compared with the bulk carbon steel, the time constant of Fe thin films shifted to a lower frequency, and the magnitudes of phase angles were smaller. This may be caused by different experimental configurations between thin films and bulk carbon steel with different current distributions. Comparing the Fe thin films, the magnitude of the maximum phase angle became smaller for thicker films. It suggests that the double layer capacitance at the film/solution interface was less ideal for thicker films, corresponding to higher roughness.^{52,53}

The LSV plots of 100 nm and 400 nm Fe thin films showed similarity to that of the bulk X65 carbon steel (Fig. 8). The cathodic region presented a limiting current for both the Fe thin films and the bulk X65, with almost the same value. The anodic LSV slope of 400 nm Fe was parallel to that of the bulk X65 when the electrode potential was < -0.5 V versus SHE. LSV slopes can reveal the corrosion mechanisms, which were discussed in detail

previously.^{5,54} As the potential became more positive, the anodic current decreased for the Fe thin films, which was different from the bulk X65. This is due to gradual dissolution and depletion of Fe thin films, reducing the material and area on the substrates for corrosion instead of passivation.

Despite the thickness effect, electrochemical corrosion of Fe thin films was in accordance with the bulk X65 in terms of E_{corr} , CR, and LSV slopes under the test conditions. This further confirms the feasibility of using Fe thin films as the corrosion proxy material. The Fe thin films were sensitive to the presence of CO₂ and pH as indicated by the significant changes in CR.

When implementing the corrosion sensor inside the pipeline, it is advisable to locate the sensor in the most susceptible locations or alternatively to enable a low-cost, distributed sensor configuration

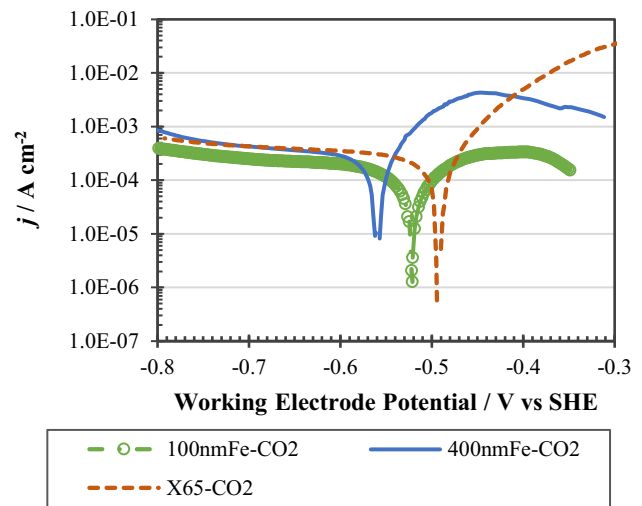


Fig. 8. LSV plots of 100 nm and 400 nm Fe thin films compared with bulk X65 carbon steel in CO₂-saturated NaCl solution at 30°C.

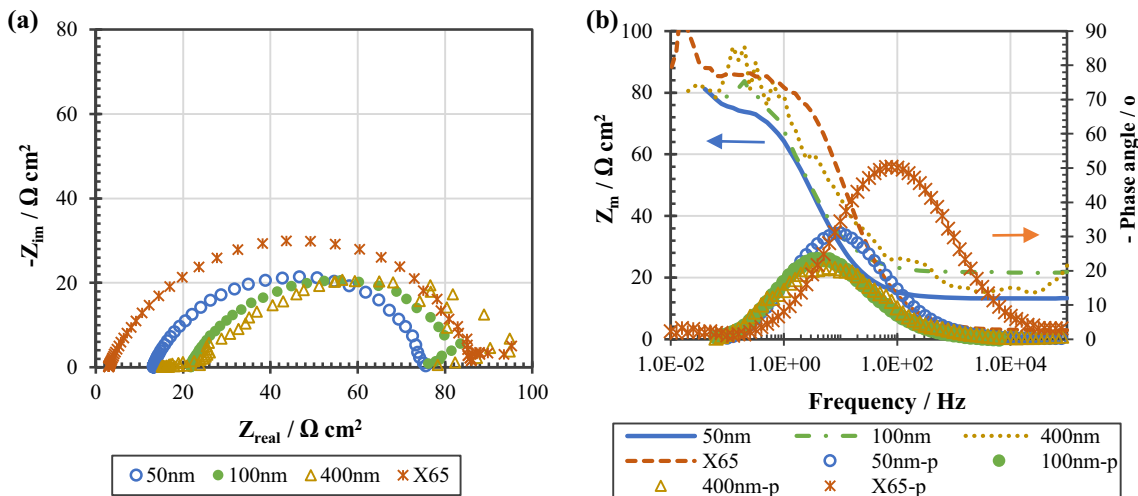


Fig. 7. (a) Nyquist and (b) Bode plots of Fe thin films compared with bulk X65 carbon steel in CO₂-saturated NaCl solution at 30°C. Symbol p represents the phase angle. Adapted from Ref. 6.

such that “at risk” segments can be identified prior to significant pipeline corrosion. Different configurations are available to integrate Fe thin films with the fiber optics to effectively take advantage of the optical fiber based sensors. For example, Fe film can be coated at the end of the optical fiber as a low-cost point sensor placed at high risk locations or can be coated along the entire fiber as a distributive sensor through more advanced sensor fabrication and interrogation methods.^{9,11,18,55}

CONCLUSION

Corrosion of Fe thin films was studied using optical and electrochemical methods and compared with the bulk carbon steel. Fe thin films were sputter deposited onto the quartz substrates, and the XPS spectrum confirms metallic Fe was successfully deposited. The AFM results showed that the average grain size and roughness increased with increasing film thickness from 25 nm to 100 nm. An oxidized top layer (1.3–1.7 nm thick) was observed because of exposure to air during the sample transport. The calculated R_s decreased as the film thickness increased.

$T\%$ of Fe thin films increased as corrosion proceeded because of the film thinning. This agrees with the optical calculation using standard Fresnel-based models of transmission in a thin film system. The $T\%$ versus time plots demonstrated a faster increase of $T\%$ in the presence of CO_2 than without CO_2 or at higher pH. Therefore, optical responses from Fe thin films can be used to monitor corrosion onset and quantify the CR.

The electrochemical results showed that CO_2 increased the CR of Fe thin films by more than one order of magnitude compared with the N_2 deaerated condition. The significant increase in CR demonstrated the high sensitivity of Fe thin films to CO_2 corrosion as a sensing material. The higher pH of ~ 6 with NaHCO_3 decreased the CR compared with pH ~ 4 . R_{pol} , CR, and E_{corr} of the Fe thin films were in good agreement with the bulk X65 carbon steel, verifying that Fe thin films can serve as a representative corrosion proxy when integrated with the optical sensing platform.

The CR increased as the film thickness increased from 25 nm to 100 nm in each solution. Although a smaller grain size in the thinner film may lead to a higher CR, the thicker film has greater surface roughness and a lower R_s , which can accelerate corrosion. The total dissolution times were consistent between the optical and electrochemical measurements.

ACKNOWLEDGEMENTS

This work was performed in support of the US Department of Energy’s Fossil Energy Crosscutting Technology Research Program and the Oil & Natural Gas Research Program. The research was executed through the NETL Research and Innova-

tion Center’s Natural Gas Infrastructure and Embedded Sensor Technology Suite for Wellbore Integrity Monitoring programs. Research performed by Leidos Research Support Team staff was conducted under the RSS contract 89243318CFE000003. Rachel English and James Egbu acknowledge the support from the NETL postgraduate program administered by Oak Ridge Institute for Science and Education (ORISE). The authors thank Mason Risley and Norman Gottron from the Nanofabrication Facility at Carnegie Mellon University for helping with Fe thin film deposition.

DISCLAIMER

This work was funded by the Department of Energy, National Energy Technology Laboratory, an agency of the United States Government, through a support contract with Leidos Research Support Team (LRST). Neither the United States Government nor any agency thereof, nor any of their employees, nor LRST, nor any of their employees, makes any warranty, expressed or implied, or assumes any legal liability or responsibility for the accuracy, completeness, or usefulness of any information, apparatus, product, or process disclosed, or represents that its use would not infringe privately owned rights. Reference herein to any specific commercial product, process, or service by trade name, trademark, manufacturer, or otherwise, does not necessarily constitute or imply its endorsement, recommendation, or favoring by the United States Government or any agency thereof. The views and opinions of authors expressed herein do not necessarily state or reflect those of the United States Government or any agency thereof

CONFLICT OF INTEREST

The authors declare that they have no conflict of interest.

SUPPLEMENTARY INFORMATION

The online version contains supplementary material available at (<https://doi.org/10.1007/s11837-020-04526-5>) contains supplementary material, which is available to authorized users.

REFERENCES

1. J.A. Beavers and N.G. Thompson, *In ASM Handb* (Materials Park: ASM International, 2006), pp. 1015–1026.
2. L.T. Popoola, A.S. Grema, G.K. Latinwo, B. Gutti, and A.S. Balogun, *Int. J. Ind. Chem.* 4, 1 (2013).
3. D. Brondel, R. Edwards, A. Hayman, D. Hill, and T. Semmerad, *Oilf. Rev.* 4, 4 (1994).

4. O. Moghissi, L. Norris, P. Dusek, B. Cookingham, and N. Sridhar, *Internal Corrosion Direct Assessment of Gas Transmission Pipelines—Methodology* (2002).
5. R.F. Wright, E.R. Brand, M. Ziomek-Moroz, J.H. Tylczak, and P.R. Ohodnicki, *Electrochim. Acta* 290, 626 (2018).
6. R.F. Wright, M. Ziomek-moroz, and P.R. Ohodnicki, in *NACE Corros.* (Phoenix, AZ, USA, 15–19 April, 2018), p. No. 10893.
7. Energy Information Administration (2020).
8. G.H. Koch, P.H. Brongers, M.N.G. Thompson, Y.P. Virmani, and J.H. Payer, *Corrosion Costs and Preventive Strategies in the United States* (NACE International, Houston, TX, USA, 2002).
9. R.F. Wright, P. Lu, J. Devkota, F. Lu, M. Ziomek-Moroz, and P.R. Ohodnicki, *Sensors* 19, 3964 (2019).
10. D. Morison, in *NACE Corros.* (2008), p. No. 08290.
11. C.K.Y. Leung, K.T. Wan, and L. Chen, *Sensors* 8, 1960 (2008).
12. P.R. Ohodnicki, S. Natesakhawat, J.P. Baltrus, B. Howard, and T.D. Brown, *Thin Solid Films* 520, 6243 (2012).
13. P.R. Ohodnicki, T.D. Brown, G.R. Holcomb, J. Tylczak, A.M. Schultz, and J.P. Baltrus, *Sensors Actuators B Chem.* 202, 489 (2014).
14. Y. Huang, Z. Gao, G. Chen, and H. Xiao, *Smart Mater. Struct.* 22, 75018 (2013).
15. C. Wang, P.R. Ohodnicki, X. Su, M. Keller, T.D. Brown, and J.P. Baltrus, *Nanoscale* 7, 2527 (2015).
16. A. Yan, Z.L. Poole, R. Chen, P.W. Leu, P. Ohodnicki, and K.P. Chen, *JOM* 67, 53 (2015).
17. C. Sun, P. Lu, R. Wright, and P.R. Ohodnicki, in *Proc. SPIE 10654, Fiber Opt. Sensors Appl. XV* (Orlando, FL, USA, 14 May, 2018), p. No. 1065405.
18. R.F. Wright, J. Egbu, P. Lu, M.P. Buric, M. Ziomek-Moroz, and P.R.J. Ohodnicki, in *NACE Corros.* (Nashville, TN, USA, 24–28 March, 2019), p. No. 13499.
19. R.F. Wright, N. Diemler, F. Lu, Y. Jee, P. Lu, J. Baltrus, M. Ziomek-Moroz, and P.R.J. Ohodnicki, in *NACE Corros.* (2020), p. No. 15051.
20. S. Li, Y.-G. Kim, S. Jung, H.-S. Song, and S.-M. Lee, *Sens. Actuators B* 120, 368 (2007).
21. G. Qiao, Z. Zhou, and J. Ou, in *Proc. 1st IEEE Int. Conf. Nano/Micro Eng. Mol. Syst.* (Zhuhai, China, 18–21 January, 2006), pp. 541–544.
22. S. Dong, Y. Liao, Q. Tian, Y. Luo, Z. Qiu, and S. Song, *Corros. Sci.* 48, 1746 (2006).
23. R. Feng, M. Ziomek-Moroz, and P.R. Ohodnicki, *OSA Tech. Dig. AM4A.2* (2017).
24. M. Stern and A.L. Geary, *J. Electrochem. Soc.* 104, 56 (1957).
25. M. Stern, *Corrosion* 14, 60 (1958).
26. S.N. Lvov, *Introduction to Electrochemical Science and Engineering*, 1st ed. (CRC Press, 2015).
27. ASTM International, *Standard Practice for Calculation of Corrosion Rates and Related Information from Electrochemical Measurements* (2010), pp. G102-89.
28. P. Wang, A. Anderko, and R.D. Young, *Fluid Phase Equilib.* 203, 141 (2002).
29. R.D. Springer, P. Wang, and A. Anderko, *SPE J.* 20, 1120 (2015).
30. H.C. Helgeson, *Am. J. Sci.* 267, 729 (1969).
31. X.L. Cheng, H.Y. Ma, J.P. Zhang, X. Chen, S.H. Chen, and H.Q. Yang, *Corrosion* 54, 369 (1998).
32. Z.A. Iofa, V.V. Batrakov, and Cho-Ngok-Ba, *Electrochim. Acta* 9, 1645 (1964).
33. D.R. Morris, L.P. Sampaleanu, and D.N. Veysey, *J. Electrochem. Soc.* 127, 1228 (1980).
34. S. Nestic, J. Postlethwaite, and S. Olsen, *Corrosion* 52, 280 (1996).
35. Y. Zheng, B. Brown, and S. Nešić, *Corrosion* 70, 351 (2014).
36. S. Nešić, *Corros. Sci.* 49, 4308 (2007).
37. M. Nordsveen, S. Nestic, R. Nyborg, and A. Stangeland, *Corrosion* 59, 443 (2003).
38. Y. Zheng, J. Ning, B. Brown, and S. Nestic, *Corrosion* 71, 316 (2015).
39. G.A. Zhang and Y.F. Cheng, *Corros. Sci.* 51, 87 (2009).
40. ASTM Standard, *ASTM Int.* E112–12 (2012).
41. D.C. Giancoli, *Physics*, 4th ed. (Prentice Hall, 1995).
42. O.S. Heavens, *Optical Properties of Thin Solid Films* (New York: Dover Publications Inc, 1991).
43. G.M. Hale and M.R. Querry, *Appl. Opt.* 12, 555 (1973).
44. I.H. Malitson, *J. Opt. Soc. Am.* 55, 1205 (1965).
45. M.A. Ordal, L.L. Long, R.J. Bell, S.E. Bell, R.R. Bell, R.W.J. Alexander, and C.A. Ward, *Appl. Opt.* 22, 1099 (1983).
46. R. Feng, S. Xu, J. Liu, and C. Wang, *Hydrometallurgy* 142, 12 (2014).
47. D. Landolt, *Corrosion and Surface Chemistry of Metals*, 1st ed. (EPFL Press, 2007).
48. F. Pessu, R. Barker, and A. Neville, *Corrosion* 71, 1452 (2015).
49. D.O. Sapiro, R. Feng, B.A. Webler, M. Ziomek-Moroz, and P.R.J. Ohodnicki, *ECS Trans.* 77, 777 (2017).
50. E.M. Pinto, A.S. Ramos, M.T. Vieira, and C.M.A. Brett, *Corros. Sci.* 52, 3891 (2010).
51. S. Jung, S. Li, and Y.-G. Kim, *Electrochem. Commun.* 8, 658 (2006).
52. E. Barsoukov and J.R. Macdonald, *Impedance Spectroscopy: Theory, Experiment, and Applications*, 2nd ed. (John Wiley & Sons, Inc., 2005).
53. R. Cabrera-Sierra, I. García, E. Sosa, T. Oropeza, and I. González, *Electrochim. Acta* 46, 487 (2000).
54. R. Feng, J.R. Beck, D.M. Hall, A. Buyuksagis, M. Ziomek-Moroz, and S.N. Lvov, *Corrosion* 74, 3 (2018).
55. S. Abderrahmane, A. Himour, R. Kherrat, E. Chailleux, N. Jaffrezic-Renault, and G. Stremmsdoerfer, *Sens. Actuators B Chem.* 75, 1 (2001).

Publisher's Note Springer Nature remains neutral with regard to jurisdictional claims in published maps and institutional affiliations.